ORIGINAL RESEARCH

Modeling and simulation of hot stamping process for medium manganese steel alloy

Oğuz Gürkan Bilir[1,2] · Tanya Aycan Başer[3] · Adem Karşı[3] · Alperen Bayram[3] · Ersoy Erişir[1,2]

Abstract

In this study, a new medium manganese (medium-Mn) steel alloy is developed for the hot stamping process and required material properties were obtained. The differences of microstructural and mechanical behaviors among typical 22MnB5 steel and medium-Mn steel are investigated during the hot stamping both in uncoated condition. The commercial Finite Element software PAM-STAMP is employed for the simulation of the hot stamping. ThermoCalc and JMatPro are used for the calculation of necessary thermophysical properties. The hot ductility and fracture behaviors of medium-Mn steel are investigated by Gleeble hot tensile experiments over the deformation temperatures of 600–900 °C and strain rates of 10^{-3} and 10^{-4} after annealing at different temperatures during the thermomechanical process. Dilatometer tests were conducted to obtain the phase transformations. Hot tensile testing and dilatometry studies indicated that the hot tensile behavior of medium-Mn steel is influenced by the microstructural alterations occurred via cooling or heating prior to the deformation. To validate the thickness distribution and the microstructural evolution, a prototype part is manufactured on a semi-industrial scale by hot stamping for both materials. A good correlation between simulation and experiments was observed. In addition, decarburization of the part is investigated. medium-Mn steel exhibited a lower decarburization layer. It was also seen that the higher hardenability of medium-Mn steel favors the martensitic transformation.

Keywords Press hardened steel · Hot stamping · Mechanical properties · Decarburization · Medium mn steel

Introduction

The number of automotive parts produced by the hot stamping process has raised dramatically in recent years leading to becoming a popular choice to produce body-in-white parts [1]. Applying the hot stamping process for producing complex-chassis parts has been limited due to low ductility of hot stamped boron steels. [2]. In recent years, researchers have worked on new processes and materials for improving the ductility of hot stamped parts. Most of these studies has been conducted on a new process design and its application in numerical simulation of hot stamping [3–8]. On the other hand, the research regarding the development of new materials for the hot stamping process are focused on typically 22MnB5 and its modifications. Zhou et al. [9] investigated a Cr-Mn modification for 22MnB5 eliminating the boron alloying and achieved 1500 MPa strength with lower C content. Another significant approach in hot stamping is the adaptation of production cycles of other AHSS grades to this method. Linke et al. [10] examined the effect of Si additions in 22MnB5 steel to adopt quench and partitioning (Q&P) treatment to the hot stamping method. In a similar study by Zhu et al. [11], a series of experiments was conducted in the combined hot stamping and Q&P process with a novel 30CrMnSi2Nb alloy. They reached a total elongation of 13% higher than < 8% of the traditional hot stamping steels at a lower tensile strength of 1380 MPa. However, the ductility level is lower in comparison to medium-Mn steels which is another candidate material for hot-stamped components. Medium-Mn steel alloys requires lower deformation temperatures compared to conventional 22MnB5 steels. Therefore, a number of studies have begun to examine warm stamping of medium-Mn steels. Detailed investigation of medium-Mn steels after warm stamping by Nam et al. [12] showed that a higher combination of strength-elongation compared to hot

✉ Tanya Aycan Başer
  tbaser@coskunoz.com.tr

1 Kocaeli University, Kocaeli, Turkey

2 OBER Research and Development Ltd, Kocaeli, Turkey

3 Coşkunöz CKM R&D Center, Bursa, Turkey

stamping of 30MnB5 steel can be achieved. Also, in similar recent research [13–15], it was concluded that warm stamping of medium-Mn steels may be promising for increasing the ductility of hot stamped parts.

Another major topic of hot stamping is the simulation and modeling of the process requiring an analysis of thermal, mechanical, and microstructural parameters correlated and interacted each other. The simulation of the hot stamping process has been performed in many studies [4, 5, 7, 8] by different approaches. However, material data about different hot stamping steels is limited. In most of the commercial software, the existing material data for the simulation of the hot stamping process is only available for 22MnB5 steel and its carbon-modified versions. On the other hand, creating original material data is relatively well not established for cold forming applications. In comparison to the hot stamping, it is rather simple to generate a new material data in the sheet metal forming simulations of cold forming. As an example, there is a large database generated by the contributions of several steel manufacturers for Autoform cold forming simulations [16].

In the hot stamping, the required material data is rather complex. The hot stamping process is a multi-step thermo-mechanical forming method consists of the following steps: (a) heating of the blanks in a heat treatment furnace, (b) holding for a finite time, (c) transferring the blank from the furnace to the forming tool, (d) closing of the forming tools, (e) holding for a finite duration to maintain martensitic formation, and (f) finally opening the tools as well as the lifting the product. Each step is crucial for the properties of the product during the multi-step thermomechanical forming cycle. Therefore, the hot stamping operation must be accurately organized to provide optimum properties for the product. For instance, if the transferring of blank to the tools is delayed, ferrite or pearlite can be formed during the cooling of the blank. Such a delay can dramatically affect the final properties of the product. The interval during transferring of blank to the tool must be kept under control [2, 17–19].

Also, the tool steels for the hot stamping are different than that used in the cold forming operations. since the main expectation for a hot stamping tool is generally the thermal conductivity. If the thermal conductivity of the tool steels is not sufficient to create a thermal difference between the blank and the tool, then the critical cooling rate necessary for a complete martensitic transformation may not be reached. To improve the cooling rate, the integrated cooling channels may provide efficient cooling. However, the cooling media, its temperature, and the cooling channel geometry along with placing in the tool are responsible for an adequate cooling rate [2–5, 7, 8, 19, 20].

During the hot stamping, the behavior of blanks is also different in comparison to the cold forming. The sheet metal forming simulations is done based on the occurrence of strain hardening in a cold deformation. On the other hand, in a hot stamping process, it must be noticed that the material properties are progressively changed through phase transformations on a heating or a cooling, since steel alloys have polymorphic transitions. Hence, the present phases such as austenite, martensite, etc. have different properties depending on the temperature. The challenge for the simulation of hot stamping is based on these simultaneous phase transformations along every process step. Besides, the phase transformations are not only relying on the temperature but also the cooling rate and the time. Therefore, a phase transformation promotes a change in mechanical properties as well as in other physical properties such as the volume and the thermal conductivity which affect the further phase transformations. On the other hand, there is a change in the thermal strain (dilatation) due to the cooling and the phase transformations since different phases have different densities. It becomes more important when the Ms temperature is achieved during the cooling because a sudden volume increase is inevitable due to the Bain distortion [2, 19, 21, 22].

Recent studies have attempted to simulate the hot stamping process and to compare it with their experimental results [23, 24]. In a work by Liu et al. [23], the FE model using PAM-STAMP was used to predict the effect of contact pressure on the properties of Al blanks. They have utilized PAM-STAMP simulated temperature evolutions to develop a model for the interfacial heat transfer coefficient between hot blanks and cold tools. Mu et al. [24] proposed a numerical model for the hot stamping process by partition heating. The part thickness was validated by experiments and a good agreement was achieved. George et al. simulated the hot forming for an industrial B-pillar part with tailored properties [7]. In their numerical analysis, the coupled thermomechanical FE models were developed with LS-DYNA to simulate the hot forming process and to predict the as-formed Vickers hardness distribution. Nevertheless, most of these studies focused on lab-scale prototypes of 22MnB5 steel as wellknown material for hot stamping. Employing the hot stamping simulation for new alloys is not well established in the literature.

In the present work, the simulation, and the validation of the hot stamping process for a newly developed medium-Mn (M-Mn) steel were studied for a complex chassis part to be used industrially. The medium-Mn steel with higher hardenability can be beneficial in the hot stamping of chassis parts since these parts have higher thickness compared to the typical thickness of hot stamped parts in body-in-white parts. In this way, a chassis part with higher strength can be provided. This paper begins by the simulation of the hot stamping process performed using the PAM-STAMP 2019.5 software package [25]. The material data required for the hot stamping process was obtained from calculated thermal and mechanical properties using ThermoCalc and

JMatPro software. In experimental work, the hot tensile tests and the deformation dilatometer experiments were performed to investigate the flow behavior and the phase transformations. Microstructural characterization was also carried out to define the phase transformations. Thus, the calculated and experimental results were used in the simulation of hot stamping. Finally, a validation of the simulation is completed.

Material and experimental procedures

Material

Two steel alloys 22MnB5 (0.23%C-1.32Mn%-0.23Si%-0.14Cr%-21ppmB, wt. pct) and medium-Mn (0.23%C-4.55%Mn-0.23%Si-0.29%Cr, wt. pct) were used in this study. A commercial hot-rolled uncoated 22MnB5 steel was delivered in 3 mm thickness. The medium-Mn steel ingot was produced by vacuum induction melting (VIM). Following a homogenization at 1200 °C for 4 h, the ingot was hot forged to produce a strip plate. The strip plate was hot rolled to a thickness of 3.5 mm with 350 mm width. The hot-rolled sheets were ground to 3 mm to remove the surface defects such as oxidation and decarburization layers before the hot stamping process. The blanks were cut from both 22MnB5 and medium-Mn steel sheets as 350×610 mm by applying Electrical Discharge Machining (EDM).

FE simulation set-up

In order to predict phase transformations depending on temperature alterations in the part and tools, the simulation of the hot stamping process was carried out by PAM-STAMP commercial simulation software hot stamping package, ESI Co. Ltd. [25]. The simulation model was created using CAD data of the designed part. In the simulation process, the simulation was consisted of six different stages: austenitization, transfer, gravity/holding, forming, quenching and cooling in air. In the first stage, austenitization temperature and time were set as 900 °C and 10 min. During the transfer stage, two different transfer times of 2 and 5 s were considered to

predict the effect of the blank transferring process on the microstructure. The gravity/holding time and the forming duration were taken as 5 s and 3 s, respectively. To predict the effect of the duration of blanks in tools on the martensitic transformation, three different quenching times were taken as 25, 35, and 50 s. After the hot stamping process, the duration of the cooling in air was taken as 5 min.

The press type is "single action with double pad tool". Prior to the transfer stage, the initial temperatures of die and punch was 70 °C, while the ambient temperature is 25 °C. A constant friction coefficient of 0.4 was used in the simulation. In addition, the convection heat transfer coefficient was used as 20 W/m^2. K and the emissivity value for radiation was taken as 0.8. The force and the closing speed of press were taken as 90 tons and 175 mm/s, respectively. As shown in Fig. 1, a finite element model for hot stamping tool is used in the simulation that make the appropriate kinematic movement to shape the part.

In order to reduce the simulation time to analyze the hot stamping process, the tool and the blank were modelled with shell elements. The minimum shell element size is 0.98 mm. Explicit method was used as finite element analysis. In Fig. 2, the mesh structure of the sheet blank is shown. The material data of tools are given in Table 1.

The thermal and material properties were attained from the PAM-STAMP material database for 22MnB5. However, the material data of newly developed medium-Mn steel was
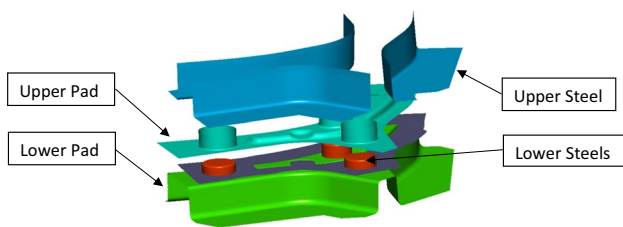

Fig. 2 Blank mesh structure

Fig. 1 Finite element model for the hot stamping tools

Table 1 Material specifications for hot stamping tools

Thermal conductivity (W/m °C)	33
Density (kg/m^3)	7800
Young's modulus (GPa)	210
Specific heat capacity (J/kgK)	650
Poisson's ratio (−)	0.3
Closing speed (mm/s)	175
Temperature (°C)	70

obtained by several experimental and modeling studies. Also, fitting of experimental data generated was used for the material properties of medium-Mn steel.

Experimental studies for material data

In this section, the experimental study for gathering the necessary phase transformation and thermomechanical properties to perform the numerical simulations of the hot stamping of chassis parts are explained. For the phase transformations, thermal dilatation, and flow curves of medium-Mn steel, the hot tensile and dilatometer tests were performed.

A Gleeble 3800 thermomechanical simulator system was used to obtain the flow curves of medium-Mn steel at different thermomechanical treatment conditions as shown in Fig. 3a. The hot tensile test specimens were cut from hot rolled medium-Mn steel using EDM. In the Gleeble simulator, the direct resistance Joule heating of hot tensile specimens was done in vacuum. The specimen dimensions were given in Fig. 3b. Temperature was monitored with thermoelements welded directly to the specimens. The dependences of flow stress on the temperature and strain rate were obtained in hot tensile tests at different temperatures (600–900 °C) and strain rates (10^{-4} and 10^{-3} s^{-1}). After hot tensile test is complete, the specimens were quenched to ambient temperatures to prevent the occurrence of softening such as recovery or recrystallization.

The hot tensile samples were divided into two groups; (a) fully austenitized and cooled to the deformation temperature or (b) only heated to the deformation temperature.
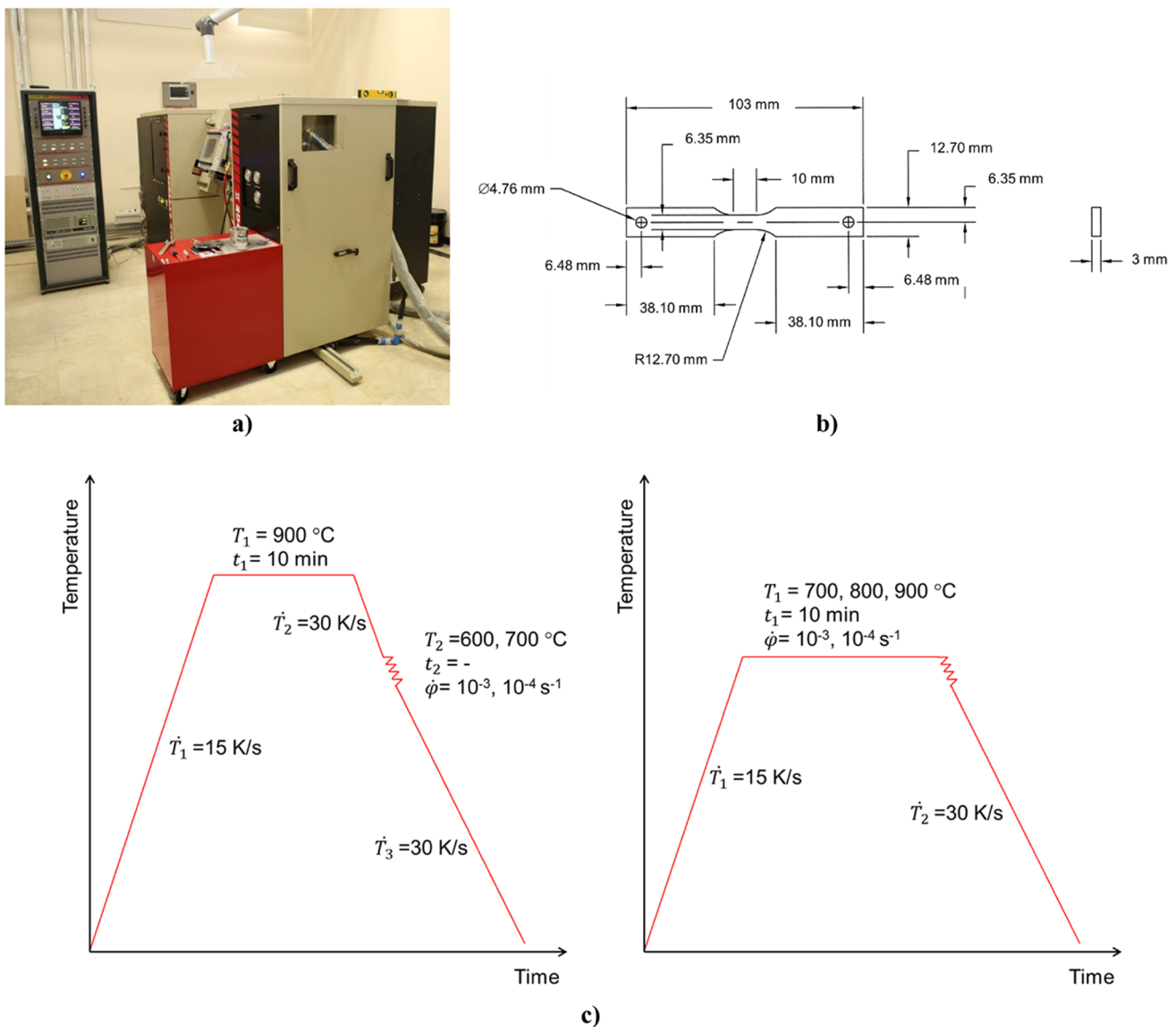

Fig. 3 Gleeble test setup (**a**), sample (**b**) and cycles (**c**) used in hot tensile tests

Thus, the effect of initial microstructure before the thermomechanical tests on the flow curve and microstructure were investigated. As schematically explained in Fig. 3c, the first group of hot tensile test specimens were heated up to 900 °C and held for 10 min to provide a fully austenitic structure and then cooled to the deformation temperatures of 700 °C and 600 °C by applying two different strain rates as 10^{-4} and 10^{-3} s^{-1}. By this approach, the first group specimens have a homogeneous austenitic microstructure prior to the thermomechanical tests. The second group was directly heated to deformation temperatures of 700 °C, 800 °C, and 900 °C and held for 10 min before applying the deformation at two different strain rates as 10^{-4} and 10^{-3} s^{-1}.

The dilatometer experiments were designed to evaluate the phase transformations and the thermal dilation by heating to 900 °C at 1.7 K/s, holding for 10 min, and then the applying a cooling at rates of 48, 32, 16, 8, and 4 K/s.

Numerical calculations for material data

In the numerical calculations, the thermal and material properties were calculated utilizing software packages Thermo-Calc and JMatPro.

22MnB5 steel is a well-known material for hot stamping. Thus, PAM-STAMP material database was used for flow curves as a function of the temperature, strain, and strain rate.

Medium-Mn steel is a new designed alloy for this work. The experimental flow curves were attained via hot tensile testing as explain above. However, a full cover of flow curves was obtained by combining the predicted flow curves and the experimental flow curves of medium-Mn steel, after the manipulation of JMatPro calculations according to the results of the hot tensile test.

The density and enthalpy values of ferrite and austenite phases of medium-Mn steel were predicted using the Thermo-Calc software and TCFE9 database based on the CALPHAD method [26]. The young modulus and thermal conductivity values were calculated using JMatPro [27].

## Experimental procedures for validation

Hot stamping process was performed using a servo press machine with a maximum press force of 980 kN. During the experimental hot stamping, the closing speed was at 175 mm/s. QRO-90 Supreme (Thermal conductivity 33 W/m °C) material is employed as a tool. The cooling channels are machined by EDM, while the hot stamping tools were manufactured via conventional CNC machining. Water is implemented as the coolant.

The austenitizing of the 22MnB5 and medium-Mn steel blanks was performed in a Bemaktherm 56 kW model heat treatment furnace with Ar atmosphere. The size of the blanks was 350 mm × 610 mm with a thickness of 3 mm. The blanks were heated to the austenitizing temperature of 900 °C at a rate of 3 K/s and held for 10 min. Then the hot blanks were manually transferred to forming tools in approx. 5 s, i.e. the time from opening the furnace to transferring hot blank to the tool surface. Once the blank was positioned, the press was closed nearly in 5 s. After the forming step is completed, the prototype parts were held in the tools for the cooling (35 and 50 s for 22MnB5 steel; 35 s for medium-Mn steel). The temperature change from the austenitization temperature to ambient temperature was measured using K-type thermoelements welded on the blank surfaces. The hot stamping of prototype parts was staged as given in Fig. 4.

Material characterization and measurements for validations

After the completion of hot stamping experiments, small samples were cut from the prototype parts and subjected to the metallographic examination to investigate cross-sections. The samples were etched at room temperature using 3% Nital to reveal the microstructure. Olympus BX51 light microscope and Jeol JSM 6060 scanning electron microscope were used for the microstructural investigation. The hardness measurements through the cross-section of the samples were carried out by Zwick Roell ZHV10 Vickers microhardness tester with 5 kg of force and dwell time of 10 s.

Fig. 4 Prototype production of chassis parts via hot stamping
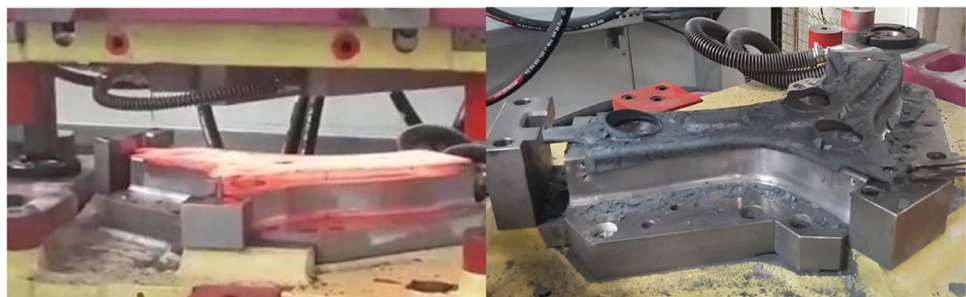
For validation studies, the thinning and carburization depth of prototype parts were determined. The thickness distribution from cross sections was compared with measured data using 3D optical measurement system. Decarburization depth was investigated according to standards on the surface decarburization of steel in **ASTM E1077-14** [28]. Microhardness was measured from the surface through the center by applying 0.2 kgf and a dwell time of 10 s.

Results and discussions

Measuring and calculating the physical and mechanical properties for the simulation

The critical temperatures for phase transformations were obtained using the dilatometry technique for medium-Mn steel. The measured Ms temperatures depending on the cooling rate were listed in Table 2 along with A_{C1} and A_{C3} temperatures. In PAM-STAMP simulations, the average values of measured Ms and A_{C3} temperatures were used as the input. In medium Mn steels the dilatation behavior during heating is dramatically different than a low alloy steel which has a noticeable difference between lowest temperature that austenite is started to be formed (A_{C1b}) and the highest temperature that cementite is available (A_{C1e}). In

PAM-STAMP simulation these two temperatures are not as important as Ac3 temperature which points the lowest temperature that microstructure becomes fully austenite and Ms temperature which points the starting of martensite formation. However, these two temperatures are very important the understand the relying mechanism of the variability in hot ductility behavior since it explains the corresponding microstructures during hot deformation. Therefore, A_{C1b} is used as Ac1 since it is the beginning of austenite formation during heating along with Ms and A_{C3} temperatures. Cooling rate is another important parameter to be used in simulation since it indicates the hardenability behavior of the material during cooling. According to the results, the martensitic transformation can be obtained at relatively slow cooling rates above 4 K/s. The measured Ms temperatures are also close to each other with a standard deviation of 2.5 °C.

The effect of deformation temperature, strain rate, and annealing temperature on the flow properties of medium-Mn steel have been investigated via hot tensile tests. The results were summarized in Table 3 and true strain-stress curves were illustrated as in Fig. 5. It can be seen that the annealing temperature has a significant effect on the true stress-strain curves.

The maximum tensile stress (MTS) decreases with increasing deformation temperature. After the hot tensile testing at 700 °C and 10^{-3} s^{-1}, the MTS was measured as 163.93 MPa, however it was dropped to 89.66 and 55.44 MPa by increasing the deformation temperatures to 800 and 900 °C, respectively. Similar decrease was observed in decreasing the strain rate to 10^{-4} s^{-1}. At the deformation temperatures of 800 and 900 °C, the MTS were 60.81 and 33.95 MPa, respectively. However, it must be noticed that the strain rate has noticeable effects on the stress-strain curves for all temperatures. The MTS was measured nearly 1.5 times higher for a strain rate at 10^{-3} s^{-1} compared to a strain rate at 10^{-4} s^{-1} for the same annealing temperature. A continuous flow curve was observed for all samples.

According to the critical values from stress-strain curves in Table 3, a significant difference was not observed in the MTS whether the deformation is carried out after cooling
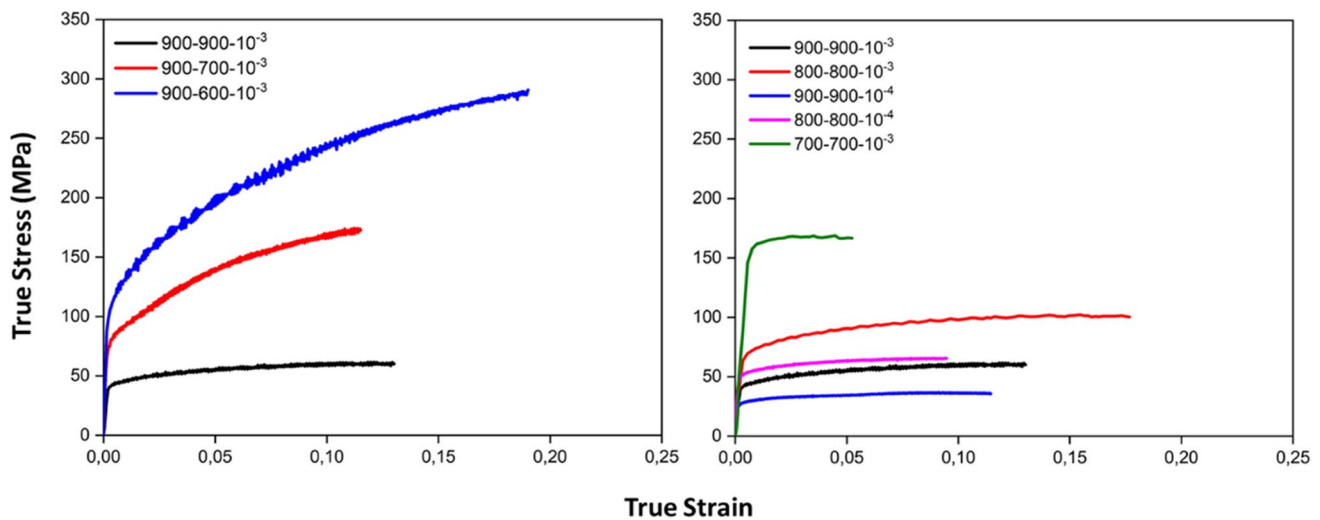
Table 2 Measured critical temperatures for medium-Mn steel by dilatometer (average and standard deviation values are given in bold)

Cooling Rate (K/s)		Critical Temperatures (°C)		
	Ms	Ac$_{1b}$	Ac$_{1e}$	Ac$_3$
4	326.4	626.9	745.5	806.4
8	326.5	623.8	745.6	816.9
16	321.6	606.8	741.4	817.0
32	321.2	631.1	744.5	813.7
48	324.0	629.9	744.2	818.9
Average	**323.9**	**623.7**	**744.2**	**814.6**
Standard deviation	**2.5**	**9.9**	**1.7**	**4.9**

Table 3 Measured maximum true stress and elongation values for medium-Mn steel measured by Gleeble

Samples	Annealing temperature (°C)	Deformation temperature (°C)	Strain rate (s^{-1})	Ultimate Tensile stress (MPa)	Uniform elongation % (-)	Total elongation % (-)
900-900-10^{-3}	900	900	10^{-3}	55.44	7.48	40.62
900-900-10^{-4}	900	900	10^{-4}	33.95	7.42	33.34
800-800-10^{-3}	800	800	10^{-3}	89.66	10.23	47.23
800-800-10^{-4}	800	800	10^{-4}	60.81	8.28	34.80
700-700-10^{-3}	700	700	10^{-3}	163.93	2.62	10.22
900-700-10^{-3}	900	700	10^{-3}	158.37	15.93	40.49
900-600-10^{-3}	900	600	10^{-3}	240.39	20.97	41.23

Fig. 5 True stress-strain curves for medium-Mn steel at different annealing temperatures as 900, 800, 700 °C, cooling temperatures as 900, 700, 600 °C and strain rates as 10^{-3} s^{-1} and 10^{-4} s^{-1} (Samples are named as annealing temperature-cooling temperature-strain rate)

or heating to deformation temperature. When the deforming at 700 °C after the holding at 900 °C or without the annealing, the MTS values were measured as 158.37 MPa and 163.93 MPa, respectively. This can be related to similar mobility of dislocations at the same temperature. On the other hand, a dramatic drop was observed for the total elongation (TE) values. It was measured as 10.22% for the sample heated to 700 °C, while it was measured as 40.49% for the sample cooled to 700 C. The variation of the TE values can be explained by the phase transformations upon the heating and the cooling. The flow curves at 700 °C which is below the A_{C3} temperature of medium-Mn steel, were obtained after two different annealing cycles via the heating from ambient temperature and the cooling from 900 °C. Thus, in the first case at a temperature below A_{C3}, a full austenitization was not formed. The second cycle, however, starts from a fully austenitic structure and phase transformation may not occur when it is cooled to 700 °C.

This finding was unexpected and suggests that the hot ductility is largely affected by prior microstructure while the MTS remains almost constant. However, it is in agreement with previous studies. Lee et al. examined 22MnB5 steel by applying austenitization at 850 °C and cooling to a deformation temperature below A_{C1} as 700 °C. They observed a similar high ductility at 40% of TE [29]. In another research by Cui et al. [30], a similar high ductility level is achieved for 22MnB5 steel after cooling to 650 °C. The cooling with an austenitic microstructure or the heating with an initial microstructure containing ferrite and pearlite or martensite, to a temperature below A_{C3} temperature, are completely different conditions for the hot ductility. The main factor is the temperature for the former, while the synergistic effect of temperature and phase transformation is critical for the

latter. Güler et al. [31] studied the hot ductility behavior of USIBOR steels at various temperatures and they observed a a sudden drop for both the TE and the reduction area of specimens at 600 °C. In another study by the same authors [32] the hot ductility behavior of 30MnB5 steel was studied. They observed a decrease in TE at deformation temperatures of 700 and 800 °C. However, both studies of Güler et al. have not mentioned the possibility of having dual-phase microstructure as austenite and ferrite. Similar observations can be seen in the case of dual-phase steels with a microstructure consisted of ferrite and martensite. In dual-phase steels, the UTS can be proportionally raised by increasing the volume fraction of martensite. However, the TE does not have the same path and it is hard to predict the TE values based on the phase fraction volume fraction of martensite. A key study in this phenomenon by Tasan [33] described how the fracture was initiated at grain boundaries of ferrite and martensite due to having a multiphase microstructure. It can thus be suggested that similar behavior may be observed to heating to temperatures that a multiphase microstructure occur. On the other hand, the microstructure must be fully austenitic after the cooling to a temperature where a phase transformation does not occur. Thus, the flow curve can be only related to temperature difference.

Another significant finding of hot tensile testing can be drawn from fracture surface. According to the fracture surfaces in Fig. 6, the formation of micro voids and dimples is present. As explained above, it was found that hot ductility of medium-Mn steel is increased by increasing the strain rate. This drop at a lower strain rate can be explained by a longer time for cavities to develop around the inclusions during the ductile transgranular fracture. Also, increasing the deformation temperature to 900 °C, a higher density of
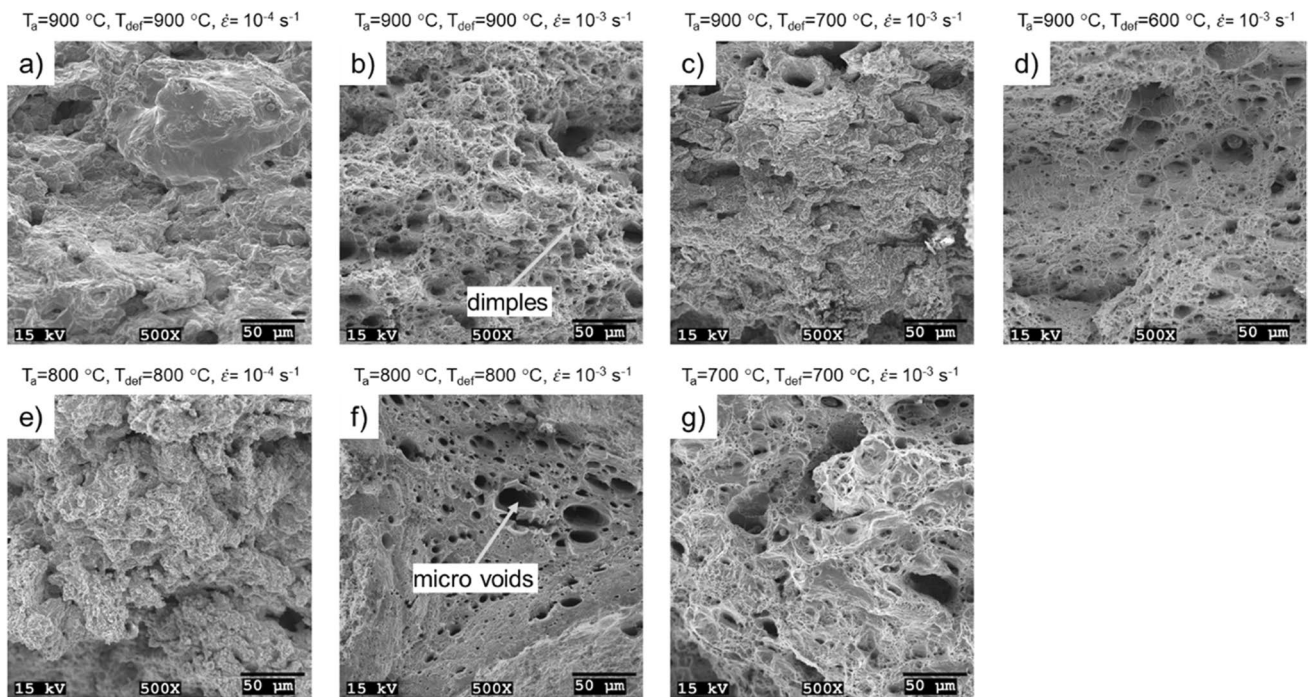
Fig. 6 Fracture surfaces of hot tensile test specimens under the conditions of (**a**) T_a=900 °C, T_{def}=900 °C, $\dot{\varepsilon} = 10^{-4}$ s^{-1}, (**b**) T_a=900 °C, T_{def}=900 °C, $\dot{\varepsilon} = 10^{-3}$ s^{-1}, (**c**) T_a=900 °C, T_{def}=700 °C, $\dot{\varepsilon} = 10^{-3}$ s^{-1}, (**d**) T_a=900 °C, T_{def}=600 °C, $\dot{\varepsilon} = 10^{-3}$ s^{-1}, (**e**) T_a=800 °C, T_{def}=800 °C, $\dot{\varepsilon} = 10^{-4}$ s^{-1}, (**f**) T_a=800 °C, T_{def}=800 °C, $\dot{\varepsilon} = 10^{-3}$ s^{-1}, (**g**) T_a=700 °C, T_{def}=700 °C, $\dot{\varepsilon} = 10^{-3}$ s^{-1} (T_a=annealing temperature, T_{def}=deformation temperature, $\dot{\varepsilon}$= strain rate)

finer voids was obtained. It is thus evident that both temperature and strain rate have influenced the fracture morphology, and hence the hot ductility. In addition, similar hot ductility behavior was observed for samples that cooled to deformation temperatures of 700 °C and 600 °C from 900 °C. This can be explained by the softening of samples by recovery and recrystallization mechanism at 900 °C prior

to deformation. However, the MTS is strongly dependent on the deformation temperature.

Physical values obtained by ThermoCalc and JMatPro were given in Figs. 7 and 8, respectively. The density and enthalpy values of ferrite and austenite phases are presented in Fig. 7. It can be seen from Fig. 8 that A_{C1} and A_{C3} temperatures are calculated differently than the measured
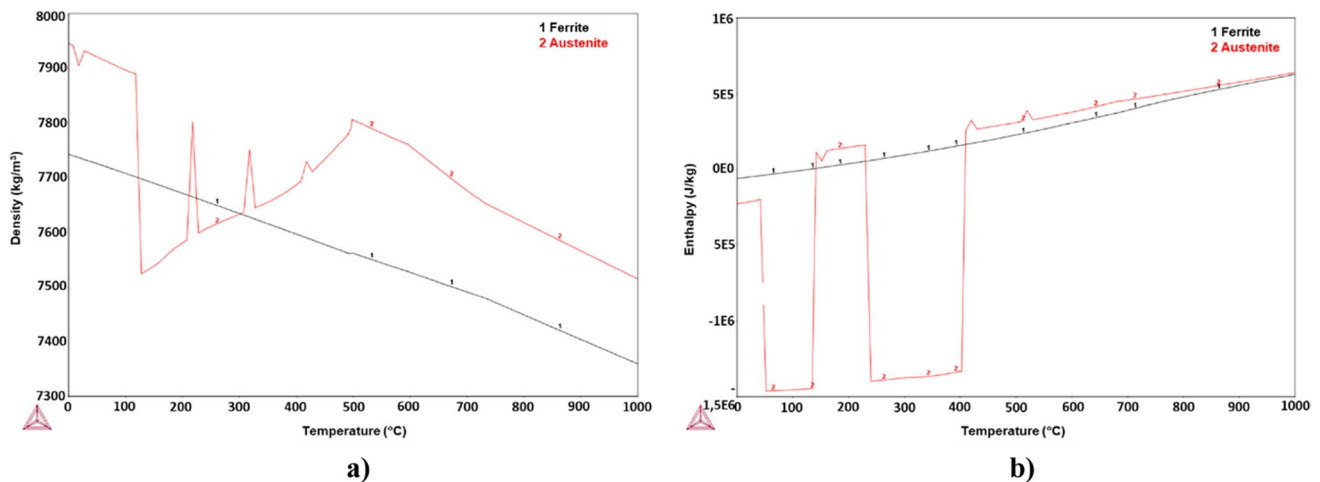

Fig. 7 Illustration of ThermoCalc calculations of (**a**) density and (**b**) enthalpy values of ferrite and austenite phases in medium-Mn steel alloy depend on temperature
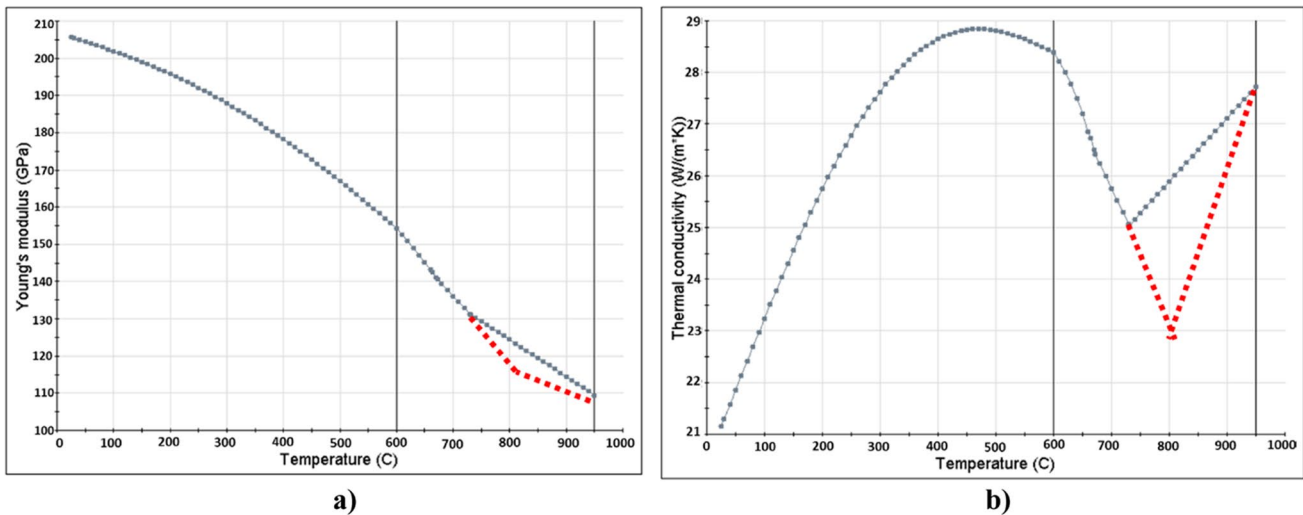
Fig. 8 Illustration of JMatPro calculations of (**a**) young modulus and (**b**) thermal conductivity values of medium-Mn steel alloy depend on temperature (red dots are the manipulated data due to having different critical temperatures for medium-Mn steel)

dilatometer results which affect the slope change points for physical properties upon temperature. Thus, the slop change points have been manipulated following the dilatometer results since the transformation temperatures are responsible for changes in the physical properties. In Fig. 8, the red dots indicate the manipulated data.

The material input data for the PAM-STAMP simulation includes various parameters. For a proper organization, the parameters for physical properties, thermal properties, and mechanical properties are described separately. Poisson ratio, Young Modulus, Density, Enthalpy, Heat Capacity and Conductivity values are called NU, E, Rho, H, Cp and K respectively for each phase and temperature. Each phase is described separately as Austenite_Rho', 'Austenite_K', 'Austenite_Cp', 'Ferrite_Rho', 'Ferrite_K', 'Ferrite_Cp'. These values are changed via the temperature as it is known, and it is described by different tables in the PAM-STAMP software such as THERMAL_E(T): E_BLANK.

The phase transformations based on temperature change are summarized in Tables 4, 5 and 6. The description of phase transformations is given in Table 4. The reconstructive and displacive phase transformations are defined by the models in PAM-STAMP according to

Jonhson-Mehl-Avrami (JMA) and Koistinen-Marburger (KM), respectively. JMA model is used to calculate both the austenite decomposition to bainite and ferrite during quenching as well as the ferrite transformation to austenite. According to the JMA model [30], the volume fractions can be predicted. The volume fraction of the diffusion-type transformation from the parent phase to the product phase is generally written as follows:

$$\frac{dP}{dt} = \frac{\bar{P} - P}{TR}$$

where P is the phase volume fraction, t is the time, $\bar{P}$ is the equilibrium value of phase volume fraction and TR is the time delay.

The volume fraction of the displacive phase transformation from austenite to martensite depends on the temperature as controlled by KM equation [34]:

$$\frac{V^\alpha}{V} = 1 - \exp[-\eta(M_s - T)]$$

Here, V^α is the volume of martensite, V is total volume, η is a constant and T is the temperature below Ms,

Table 4 Material data and descriptions in PAM-STAMP software

Phase Source	Phase Target	Described by	Model	Available Temperatures	Required Time	Phase Fraction
Austenite	Ferrite	A-F_	Jonhson-Mehl-Avrami	_PEQ	_TAU	_F
Austenite	Bainite	A-B_	Jonhson-Mehl-Avrami	_PEQ	_TAU	_F
Ferrite	Austenite	F-A_	Jonhson-Mehl-Avrami	_PEQ	_TAU	_F
Phase Source	Phase Target	Described by	Model	Ms. Temperature		
Austenite	Martensite	A-M_	Koistinen-Marburger			

Table 5 The lookup table (_PEQ) for each possible phase transformation for both materials

Material_Characterization_Curve = 'FA_peq'				
Type = Points_List	22MnB5		M-Mn Steel	
	Temperature (°C)	Availability	Temperature (°C)	Availability
ABS_ORD = 0 0	0	0	0	0
ABS_ORD = 720 0	720	0	720	0
ABS_ORD = 860 1	860	1	815	1
ABS_ORD = 1000 1	1000	1	1000	1
Material_Characterization_Curve = 'A-B_PEQ'				
Type = Points_List	22MnB5		M-Mn Steel	
	Temperature (°C)	Availability	Temperature (°C)	Availability
ABS_ORD = 0 0	0	0	0	0
ABS_ORD = 409 0	409	0	323	0
ABS_ORD = 410 1	410	1	324	1
ABS_ORD = 580 1	580	1	580	1
ABS_ORD = 581 0	581	0	581	0
ABS_ORD = 1000 0	1000	0	1000	0
Material_Characterization_Curve = 'A-F_PEQ'				
Type = Points_List	22MnB5		M-Mn Steel	
	Temperature (°C)	Availability	Temperature (°C)	Availability
ABS_ORD = 0 0	0	0	0	0
ABS_ORD = 579 0	579	0	579	0
ABS_ORD = 580 1	580	1	580	1
ABS_ORD = 730 1	730	1	730	1
ABS_ORD = 731 0	731	0	731	0

to which the sample is cooled. Thus, volume fraction martensite can be obtained from V^{α}/V.

The critical temperatures for each phase transformation were described by _PEQ as given in Table 5. Time dependency of transformations was given by _TAU values in Table 6. The data manipulation for medium-Mn steel was performed by replacing the values of 22MnB5 according to the values obtained by the dilatometer results. For instance, the A_{C3} temperature and bainite start temperature is defined as 815 °C and 324 °C, respectively. It must be noted that the medium-Mn steel has higher hardenability and transforms to martensite even at a cooling rate of 4 K/s. Thus, a bainitic or a ferritic formation during the cooling is not expected. Accordingly, the bainite and ferrite formations are manipulated in Table 6 and the starting times are shifted to 1e + 009 s.

Numerical simulation of hot stamping for 22MnB5 and medium-Mn steels

On contrary to 22MnB5 steel as the blank material of traditional hot stamping, the hardenability of medium-Mn steel is higher, and the martensitic transformation can be obtained at relatively slower cooling rates up to 4 K/s as explained in the dilatometer results. The martensite fractions after quenching are shown in Figs. 9 and 10 for the transfer times of 2

and 5 s, respectively. The blank temperature drop may vary during the transfer of the hot blank from the furnace to the tool due to the heat exchange by convection and radiation depending on the transfer time. After the hot blank contacts to the tools, the conduction becomes more crucial compared to the convection and the radiation. In the simulations, the quenching times of 25 s, 35 s, and 50 s were considered.

When a relatively shorter transfer time of 2 s was possible, it was predicted as shown in Fig. 9 that the blank of medium-Mn steel could be transformed almost completely to the martensite and remained unaffected by the quenching durations. The martensite amount is above 99% even in case of short quenching times for 25 s. On the other hand, martensite is calculated as 93% in red colored edges for 22MnB5 steel.

If the transfer time was prolonged to 5 s as indicated in Fig. 10, it is more obvious that a complete martensitic transformation could not be achieved for 22MnB5 steel. The non-martensitic areas were illustrated by white arrows in Fig. 10b. It was also seen that the quenching time between 25 and 50 s did not affect the phase transformation for both scenarios. In the case of medium-Mn steel, a complete transformation to martensite was achieved for both scenarios due to having higher hardenability.

The microstructure of samples from the experimental hot stamping of prototypes was investigated using SEM. The

Table 6 The lookup table (_TAU) for each possible phase transformation for both materials

	22MnB5 Temperature (°C)	Time (s)	M-Mn Steel Temperature (°C)	Time (s)
Material_Characterization_Curve = 'FA_tau'				
Type = Points_List				
ABS_ORD = 0 1e+009	0	1e+009	0	1e+009
ABS_ORD = 719 1e+009	719	1e+009	623	1e+009
ABS_ORD = 720 10,000	729	1e+004	624	1e+004
ABS_ORD = 760 5000	760	5e+003	760	5e+003
ABS_ORD = 880 1000	880	1e+003	880	1e+003
ABS_ORD = 950 100	950	1e+002	950	1e+002
ABS_ORD = 1000 10	1000	1e+001	1000	1e+001
ABS_ORD = 1100 1	1100	1e+000	1100	1e+000
ABS_ORD = 1250 0.1	1250	1e-001	1250	1e-001
Material_Characterization_Curve = 'A-F_TAU'				
Type = Points_List				
ABS_ORD = 0 1e+009	0	1e+009	0	1e+009
ABS_ORD = 579 1e+009	579	1e+009	579	1e+009
ABS_ORD = 580 100,000	580	1e+005	580	1e+009
ABS_ORD = 730 100,000	730	1e+005	730	1e+009
ABS_ORD = 1000 100,000	1000	1e+005	1000	1e+009
Material_Characterization_Curve = 'A-B_TAU'				
Type = Points_List	Temperature	Time	Temperature	Time
ABS_ORD = 0 1e+009	0	1e+009	0	1e+009
ABS_ORD = 409 1e+009	409	1e+009	409	1e+009
ABS_ORD = 410 10,000	410	1e+004	410	1e+009
ABS_ORD = 580 10,000	580	1e+004	580	1e+009
ABS_ORD = 1000 10,000	1000	1e+004	1000	1e+009

samples were metallographically prepared from the regions corresponding non-martensitic zones predicted for 22MnB5 steel as indicated in Fig. 11. According to the simulation results, mainly ferrite formation during the transferring of the blank is available in Zone 1. A small fraction of bainite was also predicted in Zones 2 and 3. The microstructure for medium-Mn steel was also examined in the samples from Zones 1–3. The SEM images were given in Fig. 11 for both steels.

According to comparison of calculated phases and SEM images in Fig. 11, a good correlation between calculated and experimental microstructures was seen. After SEM investigations on Zones 1–3 for 22MnB5 steel, the ferrite formation was observed in Zone 1 while a mixture of bainite and ferrite formation was observed in Zone 3 along with the martensitic matrix. In Zone 2, a small fraction of bainite was observed and the microstructure was almost fully martensitic. In the case of medium-Mn steel fully martensitic microstructure was observed in all zones.

The physical properties of blanks during hot stamping are influenced by microstructural transformations trough the temperature decrease. Therefore, after the hot stamping process, a thickness distribution over the blank is obtained. In Fig. 12, the predicted thickness distributions of blanks were given for 22MnB5 and medium-Mn steels. In the schematic diagrams, the numerical simulation results were presented for two different transfer times of 2 and 5 s after the quenching time of 25 s. Some calculated values close to average thicknesses are also indicated in Fig. 12.

In general, a higher thinning of blank for 22MnB5 steel is calculated. After the transfer time of 5 s, the minimum thicknesses were predicted as 2.263 and 2.411 mm for 22MnB5 and medium-Mn steels, respectively. Hence, the maximal thinning ratio is above 24% in 22MnB5 steel. On the other hand, the predicted thickening values are lower than 3.4 mm and comparable for both steels. The maximum thickening is predicted as 11–13%.

The quenching time is crucial on martensite transformation. If the quenching time is low, the temperature of hot stamped part can be lower than the martensite finish temperature. The cross-section of the blank was given in detail in Fig. 13 for different quenching times from 25 to 50 s. It
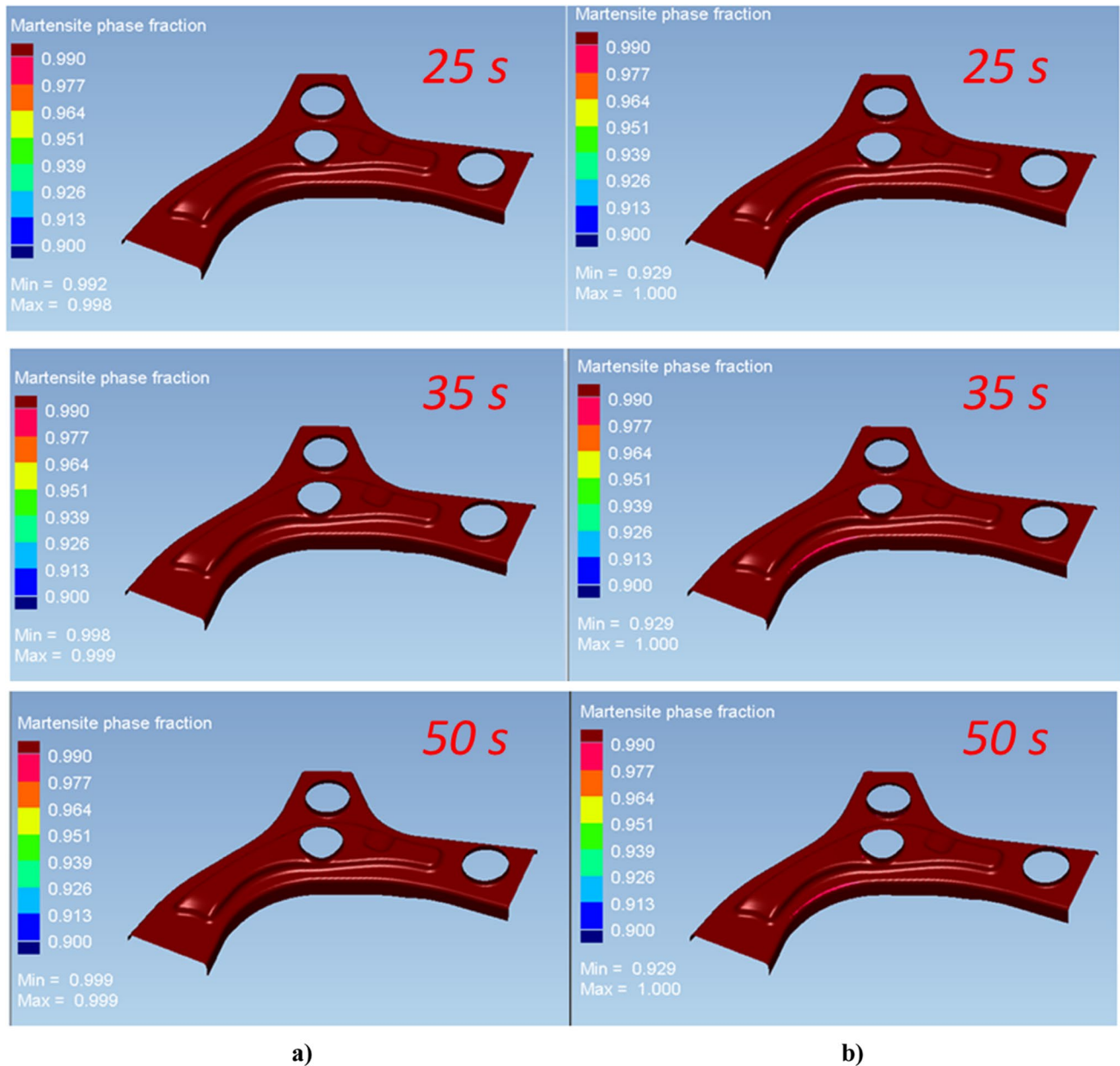
Fig. 9 Martensite fraction results after quenching for (**a**) medium-Mn steel and (**b**) 22MnB5 steel depending on different quenching times of 25 s, 35 s, and 50s (transfer time: 2 s)

can be seen that an increase in quenching time beyond 25 s barely influence the thickness of blanks for both materials. Similar result is found in a work for a typical hot stamping BR1500HS steel for quenching times from 10 to 25 s by to Zhuang et al. [35].

However, the thickness is affected along the cross sections of blanks depending on the material. In Fig. 13, yellow regions have higher thicknesses and there is a curve in geometry in this region. It is apparent from Fig. 13a that the thickening can be seen in larger zones of blanks for 22MnB5 steel.

According to Zhuang et al. [35], the thinning ratio is a crucial parameter to determine the quality of hot stamped parts and should be kept under 25%. From the numerical simulation results in Fig. 12, the maximal thinning of blank was found to be 24% for 22MnB5 steel. This value was lower than 20% for medium-Mn steel. However, these calculated results are arbitrary over the volume of blank.

To validate the simulations, a thickness distribution through the cross-section of hot stamped parts was measured using an optical measurement device for both materials. The numerical simulation results from same cross sections are
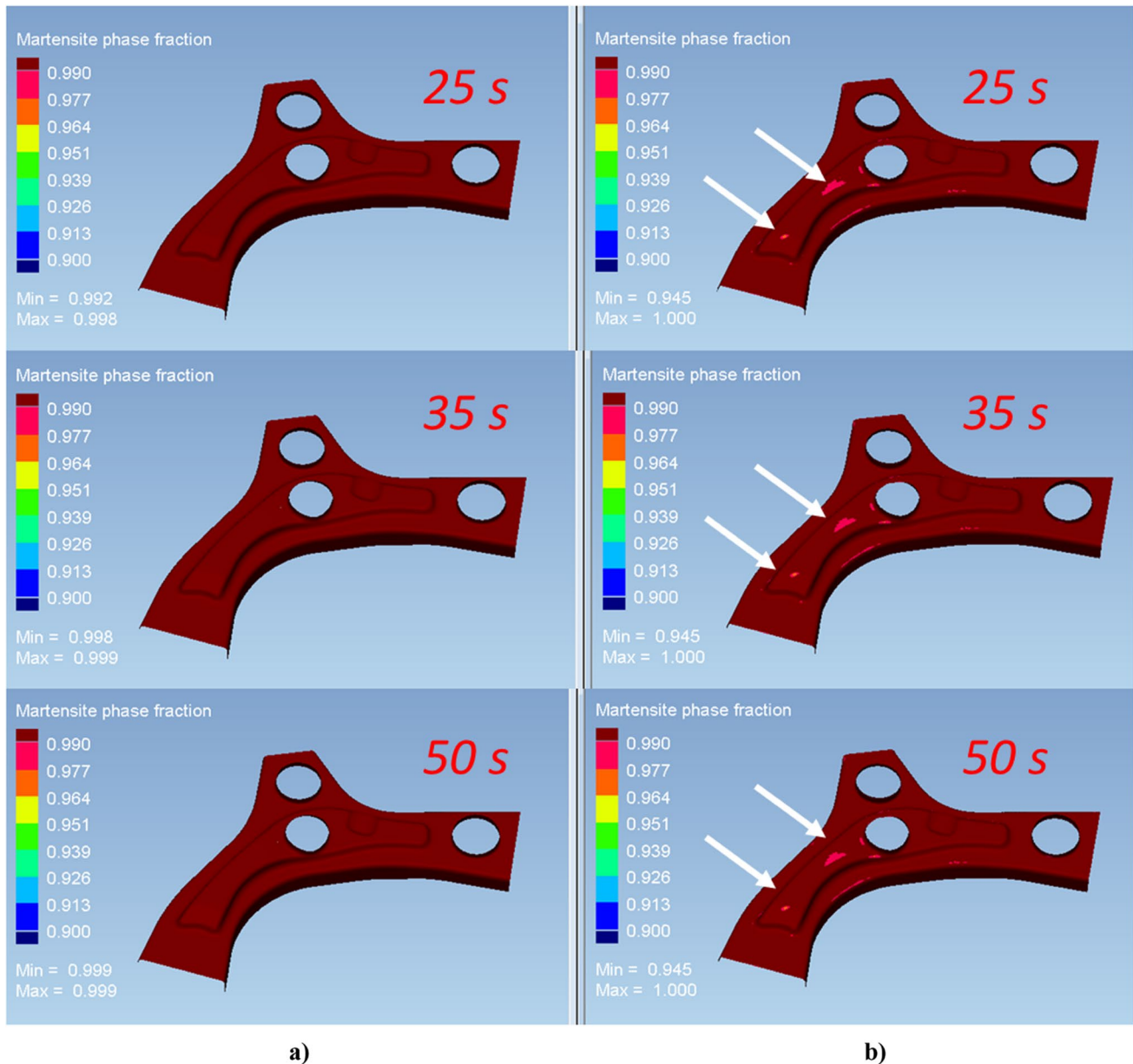
Fig. 10 Martensite fraction results after quenching for (**a**) medium-Mn steel and (**b**) 22MnB5 steel depending on different quenching times of 25 s, 35 s, and 50s (transfer time: 5 s)

considered for comparison. The calculated values were taken from the simulation conducted by applying 5 s of transfer time and 35 s of quenching time. The measured and calculated thickness distributions were given in Fig. 14.

It was found that there is a good correlation between the experimental and numerical simulation results. For medium-Mn steel, the maximal thinning from calculated and measured values are 10% and 8%, correspondingly. 22MnB5 steel has also comparable results as 9% and 10% for calculated and measured values, respectively.

On the other hand, it was seen that the thinning was higher in the section length of the cross-section from 60 m

to 120 mm for both alloys in experimental results. This result can easily be explained by the geometry of hot stamped part as seen in Fig. 13a.

Microstructural analysis of decarburization

The PAM-STAMP simulation is based on the shell element model. Therefore, the phase transformation through the thickness could not be calculated. A variety of phase transformations may occur through the thickness of the part in the hardening process. Thus, the cross-sections of Zones 1, 2, and 3 were analyzed by a light microscope to reveal
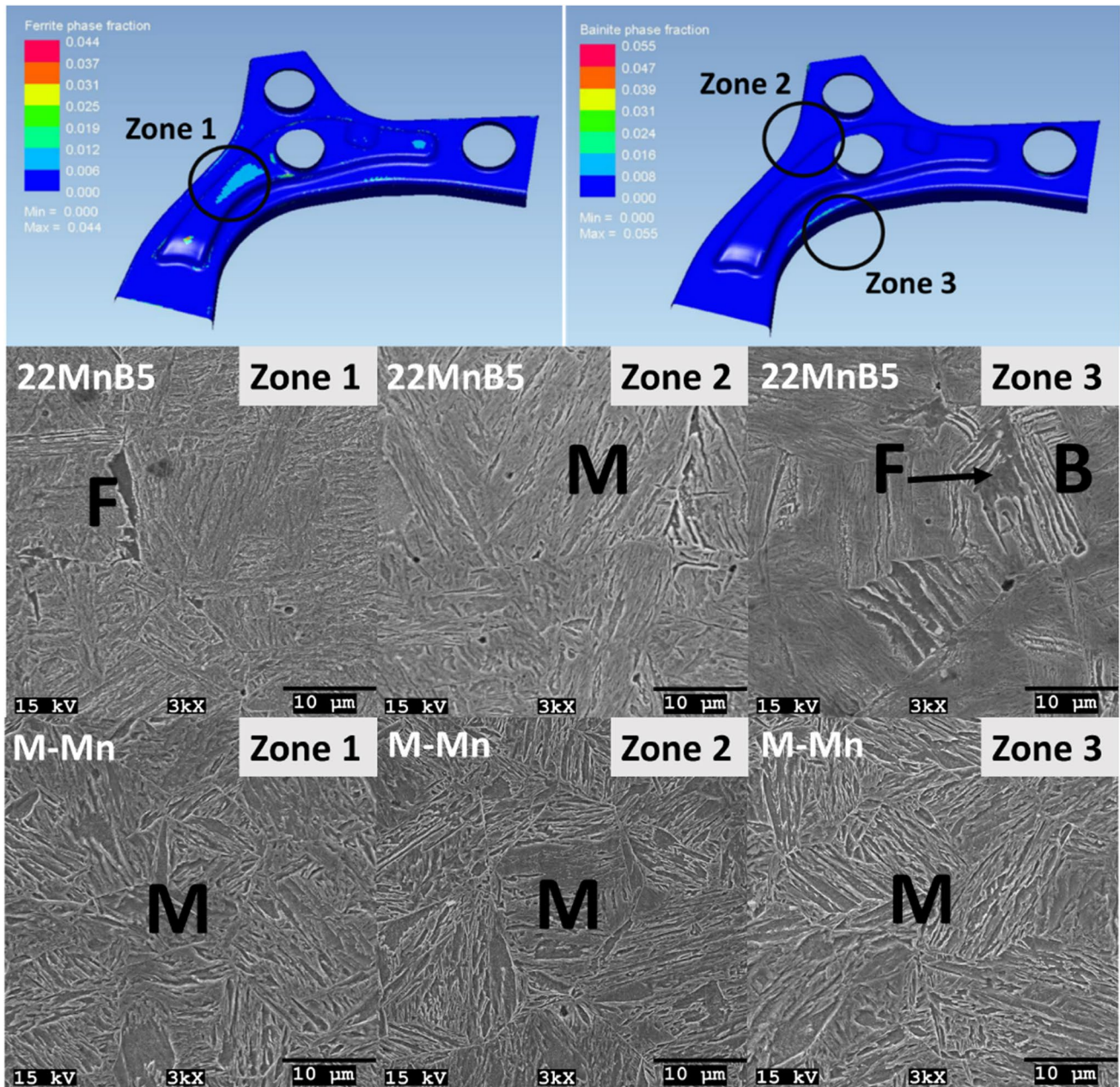
Fig. 11 Ferrite and bainite fraction results of PAM-STAMP simulation for 22MnB5 after the transfer time of 5 s and SEM micrographs for both alloys

the phase transformation through the thickness and given in Fig. 15. It was seen that there is a total decarburization (combining free-ferrite and partial decarburization) layer with a thickness of 103 μm for 22MnB5 (illustrated by a dashed line in Fig. 15), while a partial decarburization depth was seen for medium-Mn steel. The microhardness measurements from the surface to the center were carried out by applying 0.2 kgf force to further evaluate the complete decarburization layer for both alloys. Hardness and distance from the surface were illustrated as a curve with trendlines

for both alloys in Fig. 16. The hardness values from 276 HV0.2 to 619 HV0.2 were obtained in the cross-section of medium-Mn steel. However, the hardness values begin from nearly 146 HV0.2 and raise to 506 HV0.2 for 22MnB5 steel.

The micro indentation hardness method is suitable for measuring the decarburization layer when the absence of obvious microstructural changes by indicating the starting point of the plateau of hardness values from the surface to center through the cross-section of a given material. However, in high hardness levels applying smaller
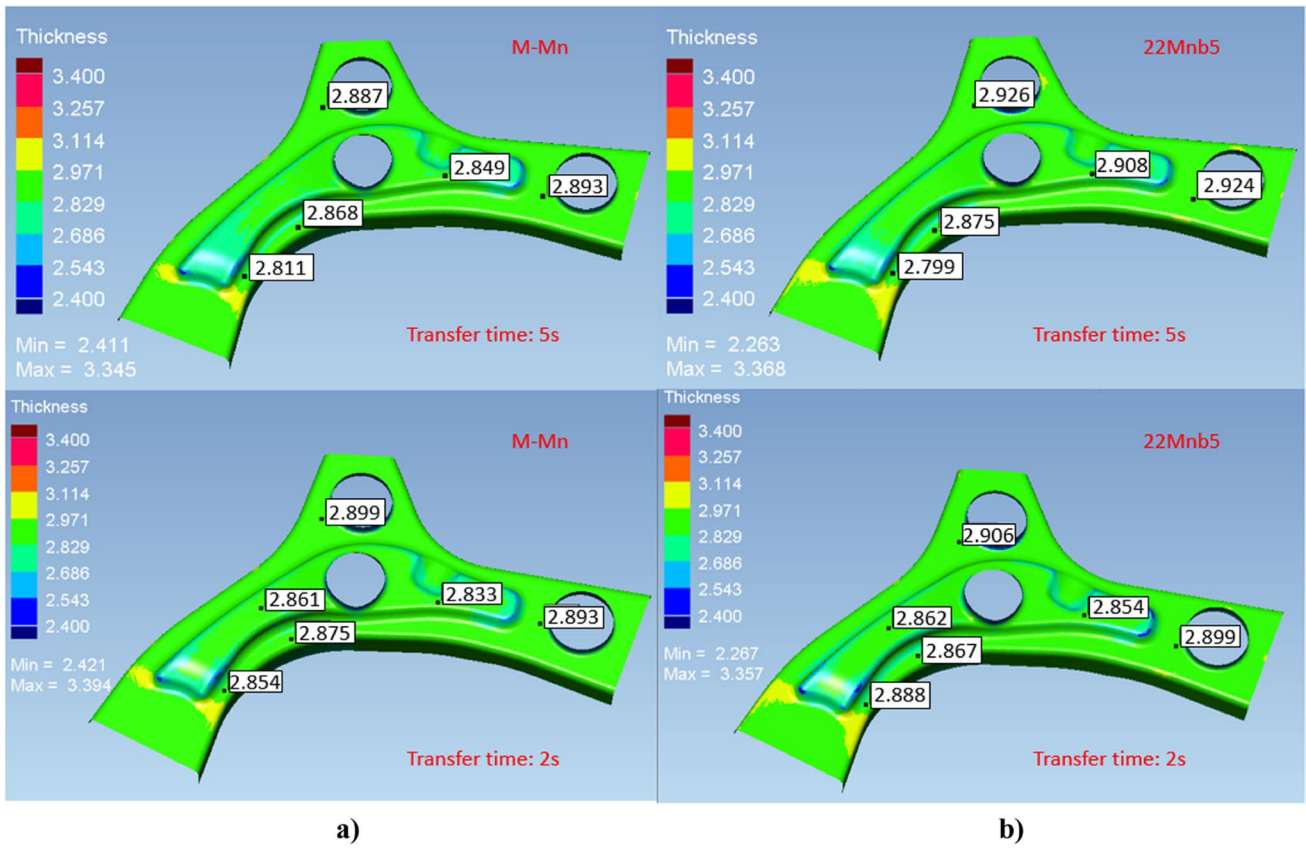
Fig. 12 Thickness distribution of blank for (**a**) medium-Mn steel and (**b**) 22MnB5 steel for different transfer times (quenching time: 25 s)
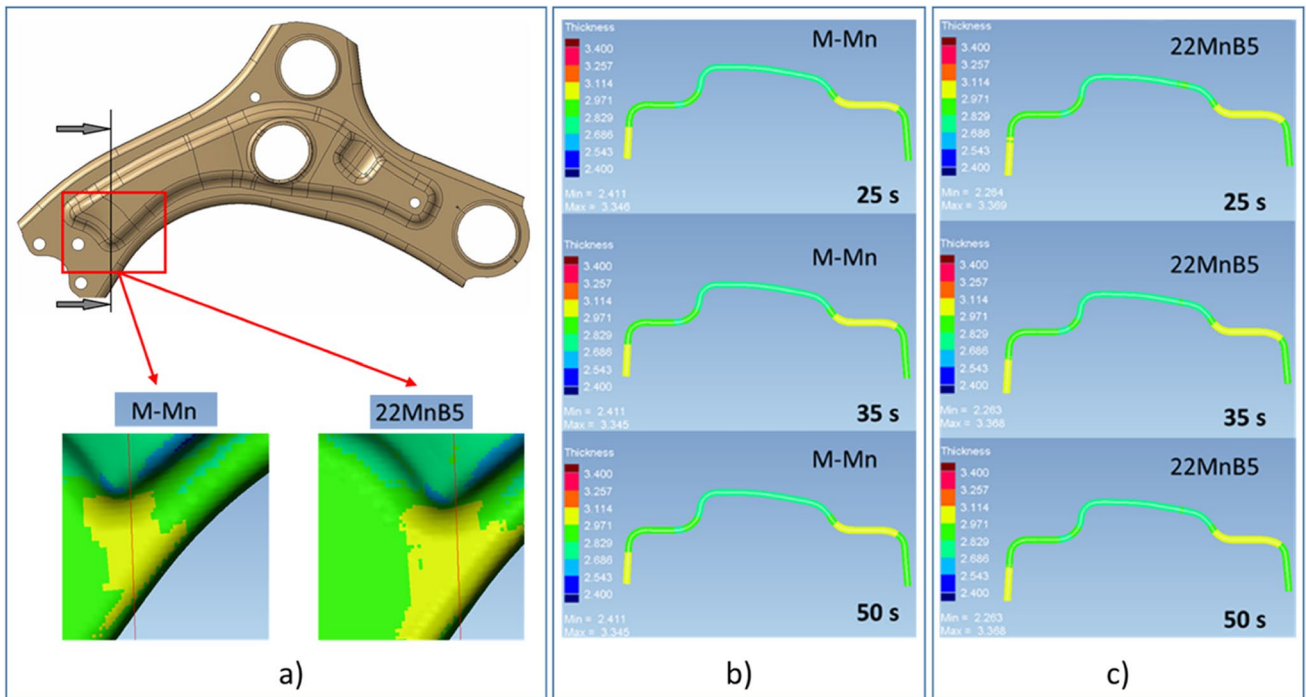

Fig. 13 Thickness distribution in (**a**) the cross-section of blank for (**b**) medium-Mn steel and (**c**) 22MnB5 steel (transfer time: 5s)

Fig. 14 Comparison of calculated and measured thickness distributions in the cross-section of blank for (**a**) medium-Mn steel and (**b**) 22MnB5 steel
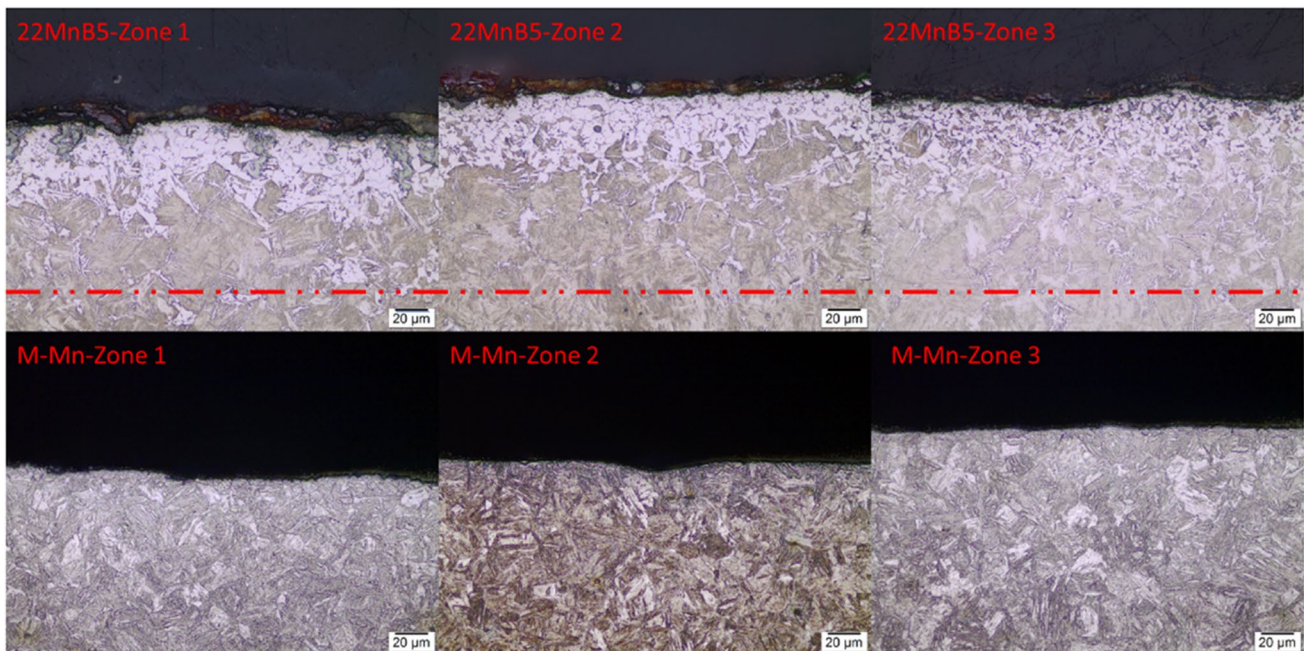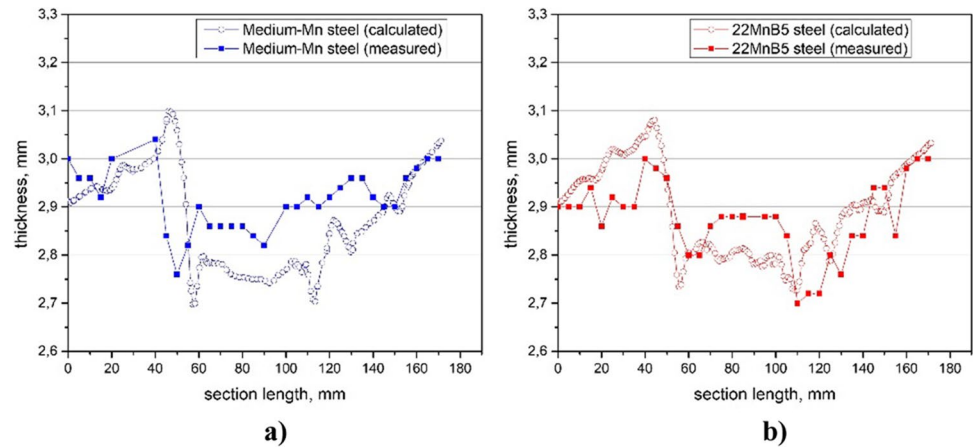

a)

b)

Fig. 15 Micrographs of 22MnB5 and medium-Mn steel for different regions after the hot stamping process

loads lowers the sensitivity since hardness depths becomes smaller. Therefore, a Vickers hardness measurement with 5 kgf was also carried out for the cross-sections (centers) of Zone 1 and Zone 2. Surface scales of the parts were gently removed by grinding to reveal the hardness of the surfaces and given in Table 7. Both alloys showed lower hardness on the surface compared to the center. The surface hardness values were 409 HV5 from Zone 1 and 472 HV5 from Zone 1 for medium-Mn steel. On the other hand, the hardness of medium-Mn steel in the center was also higher. It can be attributed to the solid solution strengthening mechanism of medium-Mn steel due to Mn alloying.

The microstructure of the decarburization layer was investigated by SEM in Fig. 17. A dual-phase microstructure with a small fraction of M/A micro constituent in a polygonal ferritic matrix was observed in the near-surface of 22MnB5 steel. A more detailed microstructure of a mixture of bainite and martensite can be seen on the surface of medium-Mn steel. Carbon depletion in the surfaces of medium-Mn steel did not lead to ferrite or dual-phase microstructure. This finding was also reported by Wang et al.. [36]. They compared hot-stamped medium-Mn steel with 22MnB5 steel. Their results indicated that 0.1 C-5Mn steel alloy warm stamped in an open atmospheric furnace showed a lower decarburization depth compared to 22MnB5 steel warm stamped in a gas-protected furnace. However, in their study, a lower austenitization temperature and shorter austenitization time were employed for medium-Mn steel and concluded that the reason behind
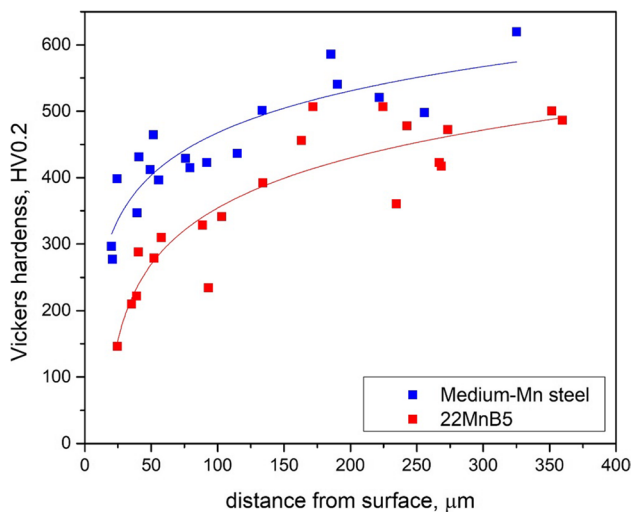
Fig. 16 Microhardness profiles for medium-Mn and 22MnB5 steels

Table 7 Hardness values were obtained from the center and surface of samples via Vickers measurements

Sample		Zone 1 (HV5)		Zone 2 (HV5)	
		Average	Deviation	Average	Deviation
M-Mn steel	Center	556	30	540	33
	Surface	520	41	474	57
22MnB5 steel	Center	409	58	472	41
	Surface	222	10	204	8

exhibiting lower decarburization is the austenitization parameters. Li et al. [37] also compared a novel medium-Mn steel (0.25 C-7.0Mn-3.29Cr) and 22MnB5 after applying the hot stamping and observed a similar lower decarburization depth for the novel alloy. They concluded that two main reasons were effective for yielding a lower decarburization depth. The former is similar to conclusions obtained by Wang et al. [36], that a shorter process time and temperature. The latter is Cr/Si/Al alloying might create a protective scale on the surface that prevents the decarburization. Thus, it must be also noted that the developed alloy in their study has a high content of alloying elements (3.29%Cr-0.38%Si-0.23%Al), which might be the reason for this conclusion. However, in our study, the same austenitization temperature and time were applied for both medium-Mn and 22MnB5 steels and yet the decarburization layer was smaller.

Conclusions and discussion

Phase transformation, physical properties and hot ductility behavior of newly developed medium-Mn steel were investigated at temperatures between 600 and 900 °C and compared with 22MnB5 steel alloy. Effect of strain rate on the hot ductility behavior was also analyzed by applying strain rate values of 10^{-3} s^{-1} and 10^{-4} s^{-1}. Main conclusions can be drawn as follows:

– The experimental results indicated that the cooling to a deformation temperature from an austenitization temperature or the heating to the same deformation temperature exhibit different thermomechanical properties. Heating to a partial austenitization temperature (below A_{c3} and higher than A_{c1}) may result with a decrease in total elongation due to having two phases at test temperature.

– Deformation after immediate cooling to same temperature following the full austenitization may not result with another phase transformation based on cooling rate, the temperature that is cooled to and hardenability of the alloy. Thus, it can yield a higher total elongation. Therefore, the thermomechanical data should be taken carefully from hot tensile results for a numerical calculation by finite element analysis.

– Deformation after cooling after full austenization may also lead to phase transformation by strain inducing or phase transformation (if the hardenability is not sufficient). In such a case, a drop of total elongation might be observed. However, this situation was not observed in our case.

– It was seen that the FE software PAM-STAMP is suitable for the hot stamping process of newly developed alloys since it permits the alteration of both thermophysical and thermomechanical properties of the material. The thermodynamical and kinetic computational software packages such as ThermoCalc, JMatPro can be used for lowering the number of tests and obtaining thermophysical properties for forming simulation. According to the results of numerical simulations and experiments, a good correlation was observed for the results from the investigations of microstructure, thickness distribution, and decarburization.

– For validation of the microstructural features on a semi-industrial scale, a prototype was manufactured. Transferring of the blank from the furnace to the tool is a critical stage that a ferrite formation is inevitable for 22MnB5 steel when the transfer time is raised from 2 to 5 s. On the contrary, compared to 22MnB5 steel, medium-Mn steel is not affected by small changes in the transfer time or the quenching time owing to lower AC3 temperature and higher hardenability, respectively.

– According to the simulation and experimental results, 22MnB5 steel may include bainite and ferrite after the hot stamping. However, in the case of medium-Mn steel, there was no other phase formation than martensite. High hardenability of medium-Mn steel can be very helpful by; (1) reducing the cost of expensive tool making for hot

Fig. 17 SEM micrographs from near-surface regions of (**a**) 22MnB5 steel and (**b**) medium-Mn steel

a) b)
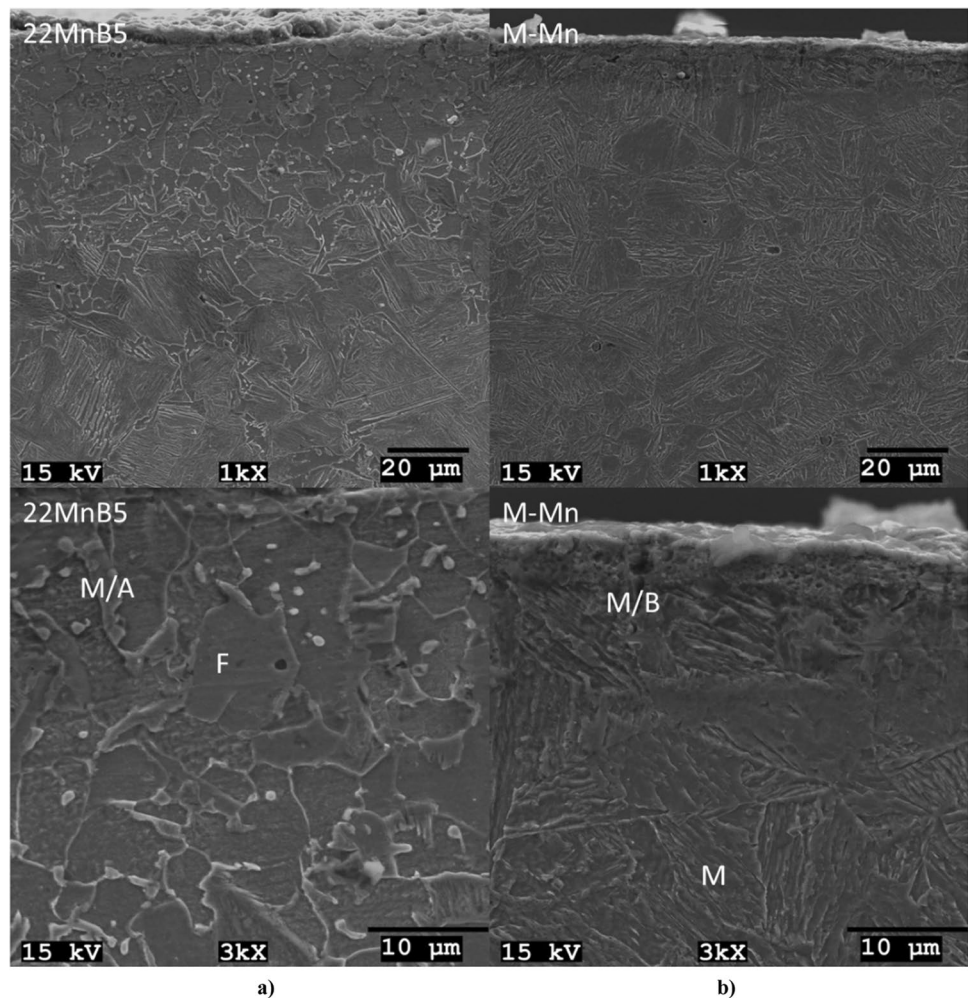
stamping since it minimizes the associated problems for insufficient cooling rate and (2) allowing for production of complex geometrical parts with higher thicknesses such as chassis parts.

– It was found that the thickness distribution of hot stamped parts can be predicted using FE software PAM-STAMP. Both materials showed similar measured and calculated thinning values as low as below 2%.

– Based to the results of microstructural investigation and microhardness testing on the decarburization layer, medium-Mn steel has a lesser hardness loss in near-surface. The microstructural characterization revealed that a bainite/martensite microstructure was dominant in the near-surface of medium-Mn steel, while 22MnB5 steel has a dual phase microstructure of decarburization ferrite and martensite. Several questions still remain to be answered to understand the underlying mechanism.

Declarations

Conflict of interest ☒ The authors declare that they have no known competing financial interests or personal relationships that could have appeared to influence the work reported in this paper.
☐ The authors declare the following financial interests/personal relationships which may be considered as potential competing interests:

References

1. Mori KI (2012) Smart hot stamping of ultra-high strength steel parts. Trans Nonferrous Met Soc China 22:s496–s503
2. Taylor T, McCulloch J (2018) Effect of part/die boundary conditions on microstructural evolution during hot stamping 2000 MPa class boron steel. Steel Res Int 89(6):1700495
3. Merklein M, Wieland M, Lechner M, Bruschi S, Ghiotti A (2016) Hot stamping of boron steel sheets with tailored properties: a review. J Mater Process Technol 228:11–24

4. Yun S, Kwon J, Cho W, Lee D, Kim Y (2020) Performance improvement of hot stamping die for patchwork blank using mixed cooling channel designs with straight and conformal channels. Appl Therm Eng 165:114562

5. Quan GZ, Zhan ZY, Zhang L, Wu DS, Luo GC, Xia YF (2016) A study on the multi-phase transformation kinetics of ultra-high-strength steel and application in thermal-mechanical-phase coupling simulation of hot stamping process. Mater Sci Eng: A 673:24–38

6. Mori K, Maki S, Tanaka Y (2009) Warm and hot stamping of ultra tensile strength steel sheets using resistance heating. CIRP Ann Manuf Technol 54 (1):209–212

7. George R, Bardelcik A, Worswick MJ (2012) Hot forming of boron steels using heated and cooled tooling for tailored properties. J Mater Process Technol 212(11):2386–2399

8. Ota E, Yogo Y, Iwata N, Nishigaki H (2019) CAE-based process design for improving formability in hot stamping with partial cooling. J Mater Process Technol 263:198–206

9. Zhou H, Zhu G, Li Q et al (2015) Microstructure and Properties of a New Cr – Mn Steel without Boron Additions for Use in Hot Stamping. Met Sci Heat Treat 57:339–343. https://doi.org/10.1007/s11041-015-9886-2

10. Linke BM, Gerber T, Hatscher A et al (2018) Impact of Si on Microstructure and Mechanical Properties of 22MnB5 Hot Stamping Steel Treated by Quenching & Partitioning (Q&P). Metall Mater Trans A 49:54–65. https://doi.org/10.1007/s11661-017-4400-7

11. Zhu B, Zhu J, Wang Y, Rolfe B, Wang Z, Zhang Y (2018) Combined hot stamping and Q&P processing with a hot air partitioning device. J Mater Process Technol 262:392–402

12. Nam JH, Han J, Lee YK (2020) The Effects of Process Temperatures on the Microstructure and Tensile Properties of Warm-Stamped Nb-Bearing M-Mn Steel. Metall Mater Trans A 51:1098–1108. https://doi.org/10.1007/s11661-019-05570-w

13. Pan HJ, Cai MH, Ding H, Huang HS, Zhu B, Wang YL, Zhang YS (2017) Microstructure evolution and enhanced performance of a novel Nb-Mo microalloyed medium Mn alloy fabricated by low-temperature rolling and warm stamping. Mater Design 134:352–360

14. Zheng G, Li X, Chang Y, Wang C, Dong H (2018) A comparative study on formability of the third-generation automotive medium-Mn steel and 22MnB5 steel. J Mater Eng Perform 27(2):530–540

15. Pan H, Cai M, Ding H, Sun S, Huang H, Zhang Y (2019) Ultra-high strength-ductile medium-Mn steel auto-parts combining warm stamping and quenching & partitioning. Mater Sci Technol 35(7):807–814

16. AutoForm Forming Material Databases. Retrieved March 20, 2022, from https://www.autoform.com/en/services/material-databases/

17. Behrens BA (2018) Hot stamping. In: Chatti S, Laperrière L, Reinhart G, Tolio T (eds) The international academy for production (eds) CIRP encyclopedia of production engineering. Springer, Berlin. https://doi.org/10.1007/978-3-642-35950-7_16722-3

18. Senuma T (2020) Hot stamping steel. In: Reference module in materials science and materials engineering. Elsevier, Amsterdam. ISBN 9780128035818. https://doi.org/10.1016/B978-0-12-803581-8.12041-7

19. Karbasian H, Tekkaya AE (2010) A review on hot stamping. J Mater Process Technol 210(15):2103–2118. ISSN 0924 – 0136. https://doi.org/10.1016/j.jmatprotec.2010.07.019

20. Hoffmann H, So H, Steinbeiss H (2007) Design of hot stamping tools with cooling system. Ann CIRP 56(1):269–272. ISSN 0007-8506. https://doi.org/10.1016/j.cirp.2007.05.062

21. Schönbach T, Messner M, Gmainer C (2017) Press-hardening simulation-the next level of maturity. J Phys: Conf Ser 896(1):012062. IOP Publishing. https://doi.org/10.1088/1742-6596/896/1/012062

22. Hagenah H, Merklein M, Lechner M, Schaub A, Lutz S (2015) Determination of the mechanical properties of hot stamped parts from numerical simulations. Procedia Cirp 33:167–172. https://doi.org/10.1016/j.procir.2015.06.031

23. Liu X, Ji K, El Fakir O, Fang H, Gharbi MM, Wang L (2017) Determination of the interfacial heat transfer coefficient for a hot aluminium stamping process. J Mater Process Technol 247:158–170

24. Mu Y, Zhou J, Wang B, Wang Q, Ghiotti A, Bruschi S (2018) Numerical simulation of hot stamping by partition heating based on advanced constitutive modelling of 22MnB5 behaviour. Finite Elem Anal Des 147:34–44

25. ESI Group. Technical paper, from part design to part production - Virtual hot forming engineering illustrated – Focus material modelling. ESI Group, Paris

26. Andersson JO, Helander T, Höglund L, Shi P, Sundman B (2002) Thermo-Calc & DICTRA, computational tools for materials science. Calphad 26(2):273–312

27. Saunders N, Guo UKZ, Li X, Miodownik AP, Schillé JP (2003) Using JMatPro to model materials properties and behavior. Jom 55(12):60–65

28. ASTM E1077-14; Standard test methods for estimating the depth of decarburization of steel specimens

29. Lee CW, Fan DW, Sohn IR, Lee SJ, De Cooman BC (2012) Liquid-metal-induced embrittlement of Zn-coated hot stamping steel. Metall Mater Trans A 43(13):5122–5127. https://doi.org/10.1007/s11661-012-131

30. Cui J, Sun G, Xu J, Huang X, Li G (2015) A method to evaluate the formability of high-strength steel in hot stamping. Mater Design 77:95–109. https://doi.org/10.1016/j.matdes.2015.04.009

31. Hande Güler R, Ertan R, Özcan (2014) Investigation of the hot ductility of a high-strength boron steel. Mater Sci Eng A 608:90–94. ISSN 0921–5093. https://doi.org/10.1016/j.msea.2014.04.053

32. Güler H Ertan R, Özcan R (2013) Characteristics of 30MnB5 boron steel at elevated temperatures. Mater Sci Eng A 578:417–421. ISSN 0921–5093. https://doi.org/10.1016/j.msea.2013.04.116

33. Tasan CC, Diehl M, Yan D, Bechtold M, Roters F, Schemmann L, Raabe D (2015) An overview of dual-phase steels: advances in microstructure-oriented processing and micromechanically guided design. Annu Rev Mater Sci 45:391–431. https://doi.org/10.1146/annurev-matsci-070214-021103

34. Koistinen DP, Marburger RE (1959) A general equation prescribing the extent of the austenite-martensite transformation in pure iron-carbon alloys and plain carbon steels. Acta Metall 7:59–60

35. Zhuang BL, Shan ZD, Jiang C, Li XY (2014) Control over mechanical properties and microstructure of BR1500HS hot-stamped parts. J Iron Steel Res Int 21(6):606–613

36. Wang C, Li X, Han S, Zhang L, Chang Y, Cao W, Dong H (2018) Warm stamping technology of the medium manganese steel. Steel Res Int 89(9):1700360

37. Li S, Wen P, Li S, Song W, Wang Y, Luo H (2021) A novel medium-Mn steel with superior mechanical properties and marginal oxidization after press hardening. Acta Materialia 205:116567